*J. Fluid Mech.* (1995), *vol.* 288, *pp.* 325–350



# An experimental study of the onset of parametrically pumped surface waves in viscous fluids

By JOHN BECHHOEFER, VALERIE EGO, SEBASTIEN MANNEVILLE AND BRAD JOHNSON

Department of Physics, Simon Fraser University,
Burnaby, British Columbia, V5A 1S6, Canada

(Received 7 June 1994 and in revised form 22 November 1994)

We measure the threshold accelerations necessary to excite surface waves in a vertically vibrated fluid container (the Faraday instability). Under the proper conditions, the thresholds and onset wavelengths agree with recent theoretical predictions for a laterally infinite, finite-depth container filled with a viscous fluid. Experimentally, we show that by using a viscous, non-polar fluid, the finite-size effects of sidewalls and the effects of surface contamination can be made negligible. We also show that finite-size corrections are of order $h/L$, where $h$ is the fluid depth and $L$ the container size. Based on these measurements, one can more easily interpret certain unexpected observations from previous experimental studies of the Faraday instability.

## 1. Introduction

In this paper, we measure the onset of parametrically pumped surface waves in a setting commonly known as the Faraday instability (Faraday 1831). A container of fluid, paraffin oil in our case, is vertically vibrated at a given frequency and amplitude. Above an acceleration threshold, waves spontaneously appear at the surface of the fluid, vibrating at precisely half the driving frequency. In a large box, the wavelength at onset is well-defined. We measure both the acceleration threshold and onset wavelength as a function of the driving frequency, fluid properties, and sample geometry.

There are two reasons for undertaking this study. Previous investigations of thresholds have often disagreed with theoretical predictions or have required uncontrolled parameter fits, with no test as to the accuracy of the parameters deduced. Additional physical processes were also postulated with no test as to their relevance. (See §3, below.) Second, an understanding of linear-stability analysis is a prerequisite for exploring the nonlinear regime and can help in the interpretation of otherwise-confusing observations. (See the discussion of coherence lengths in §6, below.)

In retrospect, the poor contact between theory and experiment is not surprising, as so many physical processes were at play in many experiments that it was impossible to sort them out. Also, there was, until the recent calculation by Kumar & Tuckerman (1994), only an approximate theoretical treatment of the effects of viscosity on the instability. Although Kumar & Tuckerman compare their theory with two previous experiments (Fauve *et al.* 1992; Edwards & Fauve 1993, the arguments in the latter being presented in more detail in Edwards & Fauve 1994), the data do not cover some of

the more interesting parameter regimes and material parameters had to be fit to gain agreement.

The second reason for careful threshold measurements is linked to the use of the Faraday experiment as a setting for the exploration of general issues in pattern formation and complex dynamics. Three lines of work may be noted: (i) 'dynamical-systems' studies of the nonlinear interactions between a small number of modes that interact, often chaotically (e.g. Gollub & Meyer 1983; Ciliberto & Gollub 1984, 1985; Simonelli & Gollub 1989); (ii) onset of spatiotemporal chaos (e.g. Ezerskii, Korotin & Rabinovich 1985; Tufillaro, Ramshankar & Gollub 1989; Gollub 1991; Gluckman *et al.* 1993; Bosch & van de Water 1993); (iii) stationary pattern formation near onset (Christiansen, Alstrom & Levinsen 1992, 1995 ; Edwards & Fauve 1992, 1993; Müller 1993). As has been found to be the case in other experiments on hydrodynamic instabilities (Rayleigh–Bénard convection, Taylor–Couette flow), understanding of these dynamical phenomena is greatly enhanced if contact can be made with the fundamental equations of motion (Cross & Hohenberg 1993). Quantitative agreement between experiment and theory for thresholds is, from this point of view, the starting point for more detailed understanding of the nonlinear phenomena referred to here.

Work in the latter two categories implicitly assumes that the container size is large ('large aspect ratio'). As Edwards in particular has emphasized (private communication and Edwards & Fauve 1993), experiments conducted on low-viscosity fluids show significant finite-size effects even when the container is many wavelengths large. We shall illustrate these effects explicitly and thereby contrast the experiments on low-viscosity fluids, which give results very different from other pattern-forming systems (Cross & Hohenberg 1993), with experiments on high-viscosity fluids (Edwards & Fauve 1992, 1993; Müller 1993).

As we shall see, the main issue concerns the ways in which fluid viscosity leads to energy dissipation. Many possible contributions have been discussed and evaluated, including fluid shear localized to the surface, boundary layers at the bottom plate and sidewalls of the container, motion of the surrounding air, the moving contact line, and the surface viscosity of a surfactant film. We shall show that a proper choice of experimental fluid and of sample geometry can render all but the first insignificant. We shall also see in a systematic way how some of the other effects enter and, hence, how they may be avoided. Conducting an experiment under such conditions has the advantage that one can be confident that the physical model used is correct. (This is important if they are to be the basis for nonlinear perturbative expansions.)

In §2, we review previous theoretical work and summarize the calculation of Kumar & Tuckerman, adapted to our particular case. In §3, we review previous experimental work on threshold measurements. In §4, we describe our experimental apparatus. In §5, we present our results. In §6, we discuss the implications of these results for the design and interpretation of pattern-formation experiments. An appendix summarizes measurements of fluid properties.

## 2. Theoretical background

The first systematic exploration of surface waves on a vertically vibrated fluid was by Faraday in 1831. His very broad investigations are still worth reading today. Perhaps his most important finding was that the surface waves vibrate at precisely half the forcing frequency, a result confirmed by Rayleigh (1883*b*). The 2:1 frequency ratio between the driving pump and the response is the characteristic of parametric

resonance, where the excited modes are forced by periodically altering their proper frequency (by modulating gravity in this case). An everyday example of parametric resonance is the child's swing.

Parametric resonance is modelled by the Mathieu equation, which describes the pumping of a simple harmonic oscillator by periodic variation of its proper frequency (Landau & Lifshitz 1976, §27). A displacement $x(t)$ of a harmonic oscillator obeys

$$\ddot{x} + 2\mu\dot{x} + \omega_0^2(t)x = 0, \tag{2.1}$$

$$\omega_0^2(t) = \omega_0^2[1 + \varepsilon\cos\omega t]. \tag{2.2}$$

In (2.1), $\mu$ is the damping rate. In (2.2), $\varepsilon$ is the amplitude of the pump at frequency $\omega$. An analysis of the Mathieu equation shows that the $\varepsilon - \omega$ parameter plane is divided into regions where the amplitude $x$ goes to zero at long times (assuming finite damping) and regions ('resonance tongues') where it grows exponentially without bound. This is parametric resonance. (Nonlinear terms, of course, saturate the instability at finite amplitude.) Parametric resonance occurs for small pumping at frequency ratios $\omega/\omega_0 \approx 2/n$, for $n = 1, 2, 3, \ldots$. We refer to the odd-$n$ tongues as subharmonic and the even-$n$ tongues as harmonic. Inside the $n$th resonance tongue, the frequency of vibration is precisely $(n/2)\omega$.

When the damping $\mu = 0$, there is parametric resonance at zero $\varepsilon$ for $\omega/\omega_0 = 2/n$, but finite damping rates push up the thresholds. For the 2:1 tongue, the small-damping threshold is (Landau & Lifshitz 1976, §27)

$$\varepsilon = \frac{2}{\omega_0}\left(4\mu^2 + \delta^2\right)^{1/2} \quad \left(\frac{\mu}{\omega_0} \ll 1\right). \tag{2.3}$$

Here, $\delta = \omega - 2\omega_0$ is the detuning from exact 2:1 resonance. Note that the lowest threshold for the 2:1 tongue occurs when $\delta = 0$. Tongues with larger $n$ have larger thresholds; for small damping, they go as $\mu^{1/n}$.

Although Rayleigh (1883*a*) had suggested that the waves excited in Faraday's experiment were the result of a parametric resonance obtained by modulating gravity, it was not until 1954 that Benjamin & Ursell derived this result from the inviscid Euler equations. They showed that each normal mode of a surface wave obeys its own Mathieu equation. For a laterally infinite fluid of depth $h$, the normal modes are $e^{i\boldsymbol{k}\cdot\boldsymbol{r}}$, where $\boldsymbol{k}$ is a two-dimensional horizontal wavevector and $\boldsymbol{r} = (x, y)$. The surface of the fluid is then expanded as

$$\zeta(x, y, t) = \int_{-\infty}^{\infty} d\boldsymbol{k}\zeta_{\boldsymbol{k}}(t)e^{i\boldsymbol{k}\cdot\boldsymbol{r}}. \tag{2.4}$$

The amplitudes of the modes $\zeta_{\boldsymbol{k}}(t)$ obey Mathieu equations of the form

$$\ddot{\zeta}_{\boldsymbol{k}} + \omega_0^2(t)\zeta_{\boldsymbol{k}} = 0, \tag{2.5}$$

where the frequency of each mode is given by

$$\omega_0^2(t) = \left(g(t)k + \frac{\gamma}{\rho}k^3\right)\tanh kh. \tag{2.6}$$

Here, $k$ is the magnitude of the wavenumber $\boldsymbol{k}$, $\rho$ is the fluid density, $\gamma$ is the surface tension, $h$ is the depth of the fluid layer, and $g(t) = g - a\cos\omega t$ is the acceleration due to gravity, as measured in a reference frame moving up and down with the vertically vibrating fluid. The applied acceleration has amplitude $a$ and frequency $\omega$. Below, we

shall occasionally use the high-frequency, large-depth limit of (2.6),

$$\omega_0^2 \sim \frac{\gamma}{\rho}k^3, \tag{2.7}$$

to make numerical estimates. For parametrically excited surface waves, $\omega_0$ is just half the driving frequency $\omega$.

The derivation by Benjamin & Ursell ignores the effects of viscosity and, indeed, cannot be directly extended to include it. The traditional approach is to compute the energy dissipation of each mode based on an integral over the flow field *of the inviscid solution*, which gives $\mu = 2\nu k^2$ in laterally unbounded, deep containers. (See, for example, Miles & Henderson 1990; Milner 1991; and Miles 1993.) It turns out that this result is correct only to first order in $\nu k^2/\omega$ ($\omega$ here being the applied pump frequency). Moreover it is simply impossible, once damping is introduced, to find a set of uncoupled Mathieu equations for the amplitudes of each normal mode of the surface waves. (For small viscosities, however, one can write perturbative equations that do decouple at first order in $\nu k^2/\omega$. This fact explains why the derivation by Benjamin & Ursell was successful.) The difficulty here is a familiar one in classical mechanics: for damped oscillators, one cannot in general find uncoupled equations for time-independent normal modes (Goldstein 1980, pp. 265–268).

Recently, Kumar & Tuckerman (1994) have done a complete linear-stability analysis starting from the full Navier–Stokes equations. They use the periodicity of the external pump to write the equations as a Floquet problem, which they solve numerically. The general strategy is to use Floquet's theorem to write the vertical velocity in the form

$$v_z(z,t) = \mathrm{e}^{(s+\mathrm{i}\alpha)t}\tilde{v}_z(z,t), \tag{2.8}$$

where $\tilde{v}_z$ is periodic in time with period $2\pi/\omega$. Fourier expanding $\tilde{v}_z$, we rewrite (2.8) as

$$v_z(z,t) = \mathrm{e}^{(s+\mathrm{i}\alpha)t}\sum_{n=-\infty}^{\infty} v_n(z)\mathrm{e}^{\mathrm{i}n\omega t}. \tag{2.9}$$

Similarly, the interface position $\zeta(t)$ may be written

$$\zeta(t) = \mathrm{e}^{(s+\mathrm{i}\alpha)t}\sum_{n=-\infty}^{\infty} \zeta_n\mathrm{e}^{\mathrm{i}n\omega t}. \tag{2.10}$$

The multiplier $\alpha$ can always be chosen in the range 0 to $\omega/2$. As Kumar & Tuckerman discuss, only $\alpha = 0$ and $\alpha = \omega/2$ lead to instability; for all other values of $\alpha$, the interface is always stable. The case $\alpha = \omega/2$ corresponds to subharmonic fluid motions, while $\alpha = 0$ corresponds to harmonic fluid motions.

The next step is to substitute these forms for $v_z$ and $\zeta$ into the equations of motion. One finds a complicated equation of the form

$$A_n\zeta_n = a(\zeta_{n+1} + \zeta_{n-1}). \tag{2.11}$$

The right-hand side of (2.11) comes from expressing the forcing amplitude $a\cos\omega t$ in terms of its Fourier coefficients. It is independent of fluid properties and contains information about the forcing function only. The left-hand side, with $A_n = A_n(k, \nu, g, \gamma/\rho, s, \alpha)$ carries information concerning the fluid properties. Equation (2.11) is one of an infinite set of coupled equations, the coupling occurring through the right-hand side. To analyse the problem numerically, one can truncate the Fourier series at some maximum harmonic $N$. As Kumar & Tuckerman point out, the equations are solved most conveniently by setting the desired growth rate $s = 0$ in $A_n$

and solving for the acceleration $a$ as an eigenvalue problem. This is precisely the inverse of the strategy usually employed in linear-stability analyses, which ordinarily seek a function $s(k)$ representing the growth rate of a perturbation of wavenumber $k$. The inverse strategy is advantageous because the equations are linear in $a$ but highly nonlinear in $s$. Following Kumar & Tuckerman, the $N$ complex equations (2.11) can be written as a $2N \times 2N$ real matrix equation of the form

$$\boldsymbol{A}\zeta = a\boldsymbol{B}\zeta \tag{2.12}$$

where $\boldsymbol{A}$ and $\boldsymbol{B}$ are $2N \times 2N$ real matrices. The $\boldsymbol{A}$ matrix contains information about the fluid properties and is $2 \times 2$ block diagonal. The $\boldsymbol{B}$ matrix contains information about the parametric forcing and may be easily generalized to more complicated forcing functions, for example the two-frequency wave forms used by Edwards & Fauve (1992, 1993). Equations (2.11) may be converted to a standard eigenvalue problem by inverting $\boldsymbol{A}$, so that

$$\boldsymbol{U}\zeta = \boldsymbol{A}^{-1}\boldsymbol{B}\zeta = \frac{1}{a}\zeta. \tag{2.13}$$

The above equation is then solved numerically to a given order in $N$ using a standard eigenvalue routine.

A complete solution requires explicit expressions for $A_n$. We note that in the absence of external forcing, the derivation mirrors the one we would have done to find the dispersion relation for surface waves. Let $\mathscr{D}(\psi, k) = 0$ represent this dispersion relation, with $\operatorname{Re}\psi = s$ the decay rate and $\operatorname{Im}\psi = \omega$ the vibration frequency. The $A_n$ may then be written

$$A_n = \frac{2}{k}\mathscr{D}(\psi_n, k), \tag{2.14}$$

$$\operatorname{Re}\psi_n = s, \qquad \operatorname{Im}\psi_n = \alpha + n\omega. \tag{2.15}$$

For inviscid fluids of finite depth $h$, the dispersion function $\mathscr{D}$ is (Landau & Lifshitz 1987, p. 247)

$$\mathscr{D}_{h0}(\psi, k) = \psi^2 \coth hk + \omega_0^2. \tag{2.16}$$

For fluids of infinite depth but large viscosity, the dispersion function is (Lamb 1932, §349; Landau & Lifshitz 1987, p. 94)

$$\mathscr{D}_{\infty\nu}(\psi, k) = (\psi + 2\nu k^2)^2 + \omega_0^2 - 4\nu^2 k^3 \kappa, \tag{2.17}$$

where $\kappa^2 = k^2 + \psi/\nu$. To first order in $\nu k^2/\omega_0$, the damping rate implied by $\mathscr{D}_{\infty\nu} = 0$ is $s = -2\nu k^2$, which is the result obtained by the phenomenological theories based on the Mathieu equation. These theories do not incorporate the terms of order $\nu^2 k^4$ in (2.17) and thus are inaccurate at higher viscosities and frequencies. (At high frequencies, $\nu k^2/\omega_0 \sim \nu\omega_0^{1/3}$.)

For fluids of finite depth and large viscosity, we used the computer-algebra program Milo to find:

$$\mathscr{D}_{h\nu}(\psi, k) = \mathscr{D}_{\infty\nu}(\psi, k) - \frac{2\nu k^2(\psi + 2\nu k^2)B}{\cosh hk} + \frac{4\nu^2 k^3 \kappa \left[-\mathrm{e}^{-h\kappa} + \left(1 + (\psi/2\nu k^2)\mathrm{e}^{-hk}\right) + B\tanh hk\right]}{\sinh h\kappa}, \tag{2.18}$$

$$B = \frac{\left(1 + \psi/2\nu k^2\right)\left(\tanh h\kappa + \kappa/k\right)\mathrm{e}^{-hk} - \left(1 + \tanh h\kappa\right)\mathrm{e}^{-h\kappa}\left(\kappa/k\right)}{\tanh h\kappa - \tanh hk\left(\kappa/k\right)}. \tag{2.19}$$

One can verify that for large depth ($hk$ and $h\kappa \gg 1$), $B \to 0$ and $\mathscr{D}_{hv}(\psi, k) \to \mathscr{D}_{\infty v}(\psi, k)$.

In our own calculations, we treated the case of finite depth and viscosity, using (2.18) and (2.19). We have not treated the case of a laterally finite sample. The only boundary conditions that may readily be treated are the inconvenient 'brimful condition' and the unrealizable free boundary. The former case was first considered by Benjamin & Scott (1979) and later used for the Faraday experiment by Douady & Fauve (1988) and Douady (1990). The idea is to fill a partially wetting fluid up to the brim of the container, where the meniscus will be pinned. The at-rest solution assumed as a starting point for the above stability analysis then remains valid in this finite geometry. In practice, setting up brimful conditions is delicate. Small mechanical imperfections lead to measurable meniscus waves. A second tractable situation occurs when the contact angle remains 90° while sliding up and down the sidewalls of the container. This is not a realistic condition, since the contact angle in general varies with the velocity. Such 'contact-angle hysteresis' has been discussed by Hocking (1987). The walls then emit meniscus waves at accelerations much below the onset of parametric resonance. (The meniscus waves are directly forced by the sidewalls and oscillate at the driving frequency.) Our approach will be to find conditions where the sidewalls do not influence bulk behaviour.

The result of the stability calculation is a plot of the boundaries of stability tongues. We follow Kumar & Tuckerman and plot the tongues as a function of the wavenumber $k$ of the perturbation. Representative plots are shown in figure 1. The actual acceleration threshold is obtained by scanning over $k$ for the lowest acceleration that will produce an instability. For each plot of tongues, this gives one point. Except for very shallow depths, the 2:1 tongue has the lowest threshold. Since a continous spectrum of modes $k$ is available in the infinite container, an arbitrary pump frequency $\omega$ results in a response at $\omega/2$ with no detuning.

For finite geometries, the damping rates are increased because of shearing against the sidewalls. (If the fluid has a finite contact angle at the wall, there will be additional dissipation due to the hydrodynamic singularity at a moving contact line. See Milner 1991.) The number of modes also becomes quantized. This means that for an arbitrary pump frequency $\omega$, there no longer is automatically a fluid mode of frequency $\omega/2$. The mode that is finally excited is detuned from its proper frequency and has a higher threshold as a result. The threshold curve then has a scalloped shape, as the resonance tongue of each successive mode is explored by varying the frequency.

## 3. Previous experimental work

There have been an enormous number of experiments on the Faraday instability. Here, we restrict our attention to those that discuss thresholds. The experiments may be divided between small-aspect-ratio experiments and large-aspect-ratio experiments. We also restrict our attention to those experiments where the parametric forcing is applied to the gravitational acceleration. A number of other forcing schemes (electric, magnetic, acoustic, optical, thermal) have been reviewed by Nevolin (1984).

### 3.1. *Small-aspect-ratio experiments*

Beginning with the work of Benjamin & Ursell (1954), there have been a number of studies of thresholds in small systems. See Miles & Henderson (1990) for a review. Most of these experiments used water as a working fluid. As discussed below (see §4.1), there is almost always a contaminating film on top of water. This film lowers the

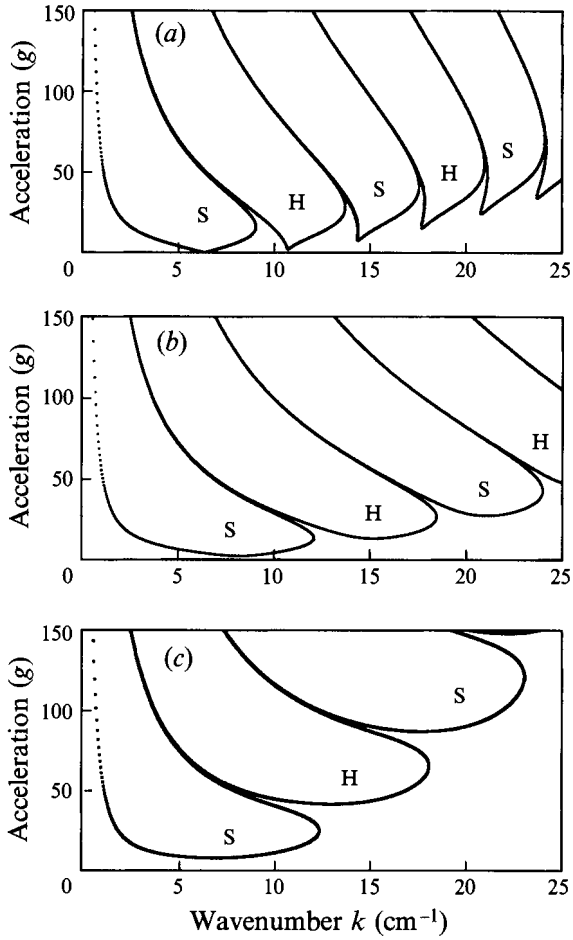


FIGURE 1. Resonance tongues calculated from the Kumar & Tuckerman (1994) theory. Note the alternating subharmonic (S) and harmonic (H) tongues. (*a*) Water at 20 °C ($\nu$ = 0.01 cm$^2$ s$^{-1}$); (*b*) oil at 55 °C ($\nu$ = 0.26 cm$^2$ s$^{-1}$); (*c*) oil at 23 °C ($\nu$ = 1.28 cm$^2$ s$^{-1}$). Note that increasing the fluid viscosity rounds the tongue bottoms and raises the thresholds. The tongues are calculated for a driving frequency of 50 Hz.

surface tension and increases the viscous damping. For example, Henderson & Miles (1990) measured the thresholds in a small cylinder and a small rectangle, using water treated with Photoflo. Although in the cylinder they found that the thresholds matched their predictions reasonably well, in the rectangle the deduced value of the viscosity was ten times that of water and the frequency dependence of the damping rate did not match their theoretical predictions. In this case, using the measured damping rate brought the measured thresholds into agreement with the predictions. (The predictions used the inviscid flow field to estimate damping by boundary layers at the top, bottom and sides of the fluid. They neglected damping caused by the surfactant film.)

Finally, Douady & Fauve (1988) and Douady (1990) studied the effect of sidewall conditions on thresholds. When the meniscus is pinned, mode-quantization effects increase greatly. They also showed that even in relatively small boxes, a continuous spectrum of modes was available if the meniscus was not pinned. In effect, when the meniscus is free to move, the boundary conditions are 'soft'. Douady made several measurements of acceleration thresholds as a function of driving frequency but he

did not attempt to compare his results to any theoretical predictions. Wavelength measurements on 'polluted' water could be well-fit to the inviscid dispersion relation and gave a surface tension of 29.5 dynes $cm^{-1}$, compared to 72.5 dynes $cm^{-1}$ for pure water.

For the small-aspect-ratio measurements, there is at best partial agreement with theoretical predictions. One reason is that in these experiments, the viscous damping due to the surface, the bottom, the sidewalls and (often) the surfactant are all important. Below, we find conditions where these effects enter separately in well-controlled ways.

### 3.2. *Large-aspect-ratio experiments*

Experiments in large cells or at high frequencies are less common than small-aspect-ratio experiments, and only a few discuss threshold measurements. Both Christiansen *et al.* (1992) and Bosch & van de Water (1993) find agreement between predicted and measured thresholds, but not enough details are provided to assess their claims. A recent manuscript by Christiansen *et al.* (1995) shows that quantitative agreement on thresholds can be obtained in a low-viscosity fluid if one is careful. They find, notably, that the energy dissipated by the moving contact line is 10–20% of the total energy dissipation. The theoretical estimates of this dissipation require knowledge of the microscopic cutoff lengths and roughness of the wall surfaces. Their values are guessed in the paper by Christiansen *et al.*, but fortunately the theory is not very sensitive to the precise values adopted.

Fauve *et al.* (1992) report observations of a $CO_2$ liquid–vapour cell near the critical point. As the authors note, the perturbative theories do not give good agreement, especially close to the critical point. These data, as well as unpublished data by Edwards & Fauve on water–glycerine mixtures, are analysed by Kumar & Tuckerman. They find good agreement in the latter case, when the surface tension and viscosity are free parameters. We note, though, that they deduce a viscosity of $\nu = 1.02\ cm^2\ s^{-1}$ while Edwards & Fauve quote $\nu = 0.85 \pm 0.05\ cm^2\ s^{-1}$. Small errors in the temperature or concentration of water could plausibly account for the differences, as could surface contamination.

Kumar & Tuckerman fit the data of Fauve *et al.* (1992) for a number of temperatures. Far from the critical point, the parameter values they deduce are in 'excellent' to 'fairly good' agreement with measured values in the literature. Closer to the critical point, they still find good threshold and wavelength fits but some parameters ($\nu$, $\eta_{liquid}$, and $\eta_{vapour}$) have not been measured. At frequencies below 20 Hz, they find discrepancies between the fit curves and the data. They suggest that sidewall damping could be responsible. Close to the critical point, mixing between the two phases and the large fluid compressibility may be important, too.

## 4. Experimental apparatus

Our apparatus is based loosely on the design of Edwards & Fauve (1992, 1993). A number of issues must be addressed in designing the experiment. These include the choice of fluid, the mechanical properties of the vibrating container, the boundary conditions, temperature control, and visualization. We consider each of these in turn.

### 4.1. *Choice of fluid*

As we have seen, many previous experiments have used water or aqueous solutions. In our opinion, this seriously complicates the interpretation of the experiments. Because

of its high surface tension, water attracts contaminants to its surface, drastically reducing the surface tension. Crudely speaking, contaminants gather at the surface because the combined water–contaminant and contaminant–air surface tensions are lower than the original water–air value. This is inconvenient because one must closely monitor the actual surface tension of the fluid used in the experiment. Water nominally has a surface tension of 72.5 dynes $\mathrm{cm}^{-1}$, but Faraday experiments using water have deduced values of 48 dynes $\mathrm{cm}^{-1}$ (Henderson, quoted in Miles 1992).

Although the large variation of surface tension is a serious problem, one might think that it suffices to measure it and use the result in the formulas quoted above. Unfortunately, this is not the only modification. As has been known since Roman times, an oily film on water greatly increases the damping of surface waves. (Experiments on this effect were carried out by Benjamin Franklin; see Tanford 1989 for a historical account and Lamb 1932, §351 and Miles 1967 for quantitative treatments.) This complicates the calculations required and means that other parameters must be measured (surface viscosity, compressibility, etc.). The simplest way around these problems is to use an oil as the working fluid. Typical surface tensions are 20 to 30 dynes $\mathrm{cm}^{-1}$ and contamination at the surface is no longer important.

Another consideration is the fluid viscosity. As Edwards & Fauve (1993) have argued, low-viscosity fluids lead to several kinds of difficulties. To have an effectively infinite container, the damping length of surface waves must be less than the container size. (One can define the damping length of a standing wave to be that of its left- and right-travelling components.) Since higher viscosities have shorter damping lengths, that is already one reason for choosing high-viscosity fluids. More precisely, if we take the damping rate to be $2\nu k^2$, then the decay length of capillary waves is, by (2.7), approximately $\ell_{decay} \approx (\frac{1}{2}\omega/k)/(2\nu k^2) \approx \gamma/(4\nu\rho\omega)$ so that one can reduce the damping length by increasing either the viscosity or the pump frequency. Since higher frequencies increase the flexing of the mechanical container, one should choose higher viscosities over higher pump frequencies. Higher viscosities require higher thresholds, since $a_c \propto \nu\omega^{5/3}$, but the tradeoff still works out in favour of higher viscosities. In addition, at small viscosities, the damping at rigid surfaces (the sides and bottom) goes as $\nu^{1/2}$ and thus dominates over the free surface damping, which goes as $\nu$ (Lamb 1932, §351).

Although high viscosities are desirable, one must be careful to check whether the fluid is non-Newtonian. This argues against certain silicone oils, which, because they are composed of long polymer molecules, readily show non-Newtonian effects. We chose instead a vacuum-pump oil (Fisher Scientific, Brand 19), which is a mixture of paraffin oils. The molecules used are relatively short chained, and the fluid remains Newtonian, even under the considerable shear that is encountered far above the onset of surface-wave motion. (Indeed, pump oils are designed to avoid 'shear thinning', a characteristic non-Newtonian effect that occurs when flow aligns otherwise-entangled molecules.) The pump oil that we chose is inexpensive, safe, and available in large batches with reproducible fluid properties. Edwards & Fauve (1992, 1993) used glycerine–water mixtures in their experiments. The high surface tension and large temperature and concentration dependence of the viscosity led us to avoid these mixtures. (In particular, that system is sensitive to the concentration shifts and gradients caused by the evaporation of water.)

In the Appendix, we detail our measurements of the relevant fluid properties (density $\rho$, surface tension $\gamma$, and kinematic viscosity $\nu$) as a function of temperature $T$. An advantage of measuring the properties 'in-house' is that we could ensure that the same temperature scale was used for all three quantities and for the actual

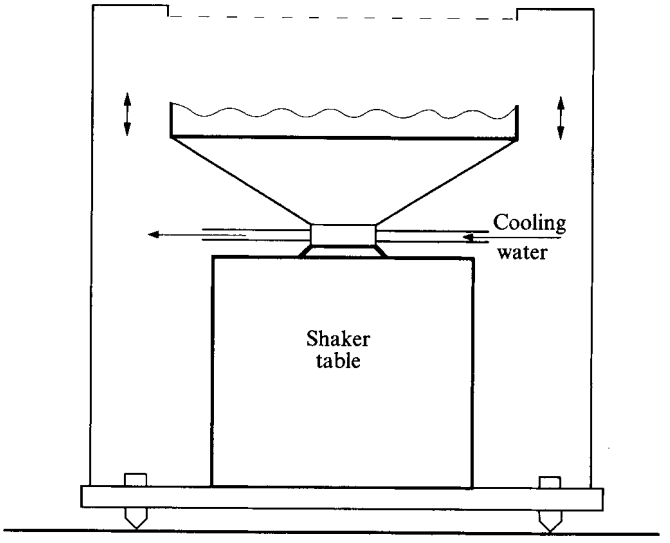


FIGURE 2. Schematic diagram of a liquid under vertical vibration.

experiment. Because of the low sensitivity of $\rho$ and $\gamma$ to temperature, varying $T$ changed in effect only $\nu$ (and hence the damping rates). This allowed us to 'scan' through another parameter in the experiment and proved useful.

### 4.2. *Mechanical properties of the container*

Our general design is sketched in figures 2 and 3. As in many previous experiments, the vibrations were generated by a shaker table (Brüel & Kjaer model 4809). Working on the same principles as loudspeakers, shakers are designed to give clean vertical motion with minimal side-to-side motion, which would cause the fluid to slosh back and forth, driving waves at accelerations below the true threshold. (We observed this motion in an early version of the experiment, which used a loudspeaker rather than a shaker table.) It is also important to eliminate container flexing, which will lead to variations in the applied acceleration over the cell. In other words, the control parameter will be spatially inhomogeneous and the instability will appear first in one part of the container and then spread to the rest of the cell. The threshold non-uniformity is an important measure of the quality of the experiment. (It is the fractional difference between the acceleration needed to destabilize one part of the cell and that needed to destabilize the cell everywhere.) In our experiment, vertical flexing was reduced by giving the bottom of the container a conical shape. Our efforts were only partially successful, and in retrospect a taller cone would have been preferable, even if it were heavier. Typical inhomogeneities ranged from 1 to 3%. One way we reduced the effects of inhomogeneities was to dynamically balance the container by adding small weights to the sides. This reduced the inhomogeneities at the cost of some tedium, since a different dynamical balancing was required for each operating frequency (for shifts of greater than 10 Hz). Nonetheless, the maximum inhomogeneity in the frequency range we used did not exceed other uncertainties, such as those arising from the measurement of oil viscosity (see the Appendix).

The shaker table was screwed into a heavy brass base 30 cm in diameter and 5 cm thick, filled with lead shot to dissipate any vibrations. Three screws were used to level the experiment. We also monitored the contact meniscus with the sidewalls for any non-uniformity.

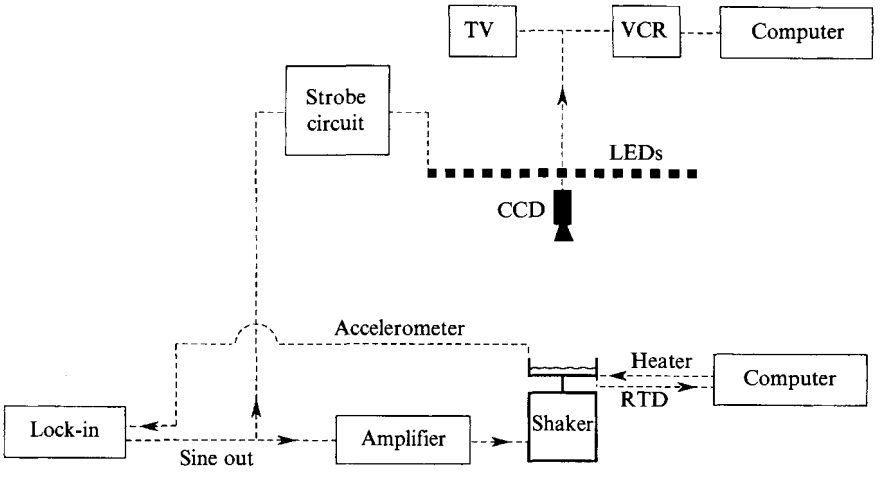


FIGURE 3. General sketch of the experimental setup.

Another concern in the mechanical design is the overall weight of the vibrating parts. Because the shaker table generates a maximum force (60 N), the maximum achievable acceleration depends on the mass that is moved. In our case, the mass of the container and fluid (at its maximum depth of 1.0 cm) was approximately 500 g, leading to accelerations of about 12 g. (Experiments conducted with shallower fluid depths could achieve as high as 17 g, although overheating of the shaker table limited the amount of time the highest accelerations could be maintained. We take $g = 9.8066\ \mathrm{m\,s^{-2}}$.) We made two aluminium sample holders, one round (inner diameter 10 cm), the other square (inner width 11.4 cm). The round container had a honeycomb array of holes drilled into the bottom to lighten the structure. A similar effect was achieved in the square container by a four-armed support attached to its underside.

The shaker table was powered by an audio amplifier (Bryston 4) that was fed the reference out sine wave from a lock-in amplifier (Stanford DSP 850; harmonics from the reference are -80 dB). The actual acceleration of the container was measured by a piezoelectric accelerometer (Brüel & Kjaer 4875) connected to a charge amplifier (Brüel & Kjaer 2634) and demodulated by the lock-in. Although the lock-in can measure the acceleration to a fractional precision of $10^{-4}$, we estimate the absolute error in the factory-provided calibration of the accelerometer to be 1%. (We checked the calibration by measuring the low-frequency displacement of the sample-holder using the displacement of a reflected laser beam.) The lock-in allowed us to assess the importance of nonlinearities in the response. At frequencies above 20 Hz, the amplitude of the second harmonic of the signal was less than 1% of the fundamental. Even when the distortions were large, there was no measurable effect on thresholds. (This is expected from theoretical considerations since the amplitude of the harmonics is always far less than that needed to destabilize the cell at that frequency.)

### 4.3. *Boundary conditions*

The boundary conditions can play an important role in determining the onset and subsequent patterns of waves. Part of our goal was to minimize the role of the boundary conditions. In the course of the experiment, we used a number of boundary conditions (see figure 4). We could switch from one boundary condition to another by gluing different inserts into the sample holder. The sample holder itself was

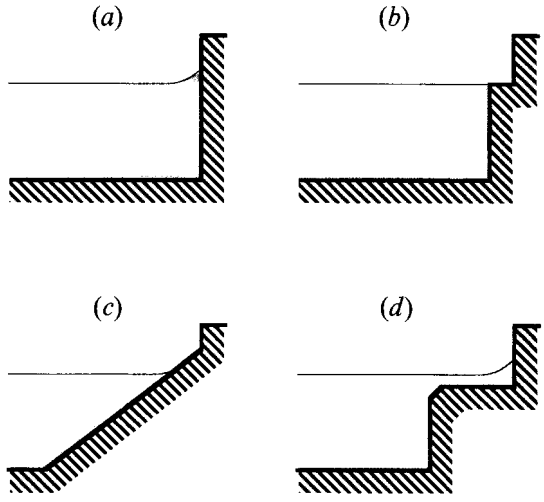


FIGURE 4. Boundary conditions. (*a*) Straight sidewalls (wetting); (*b*) brimful conditions (non-wetting fluid); (*c*) sloping sides; (*d*) shelf conditions.

made of black-anodized aluminium, which was completely wet by the oil. Unless otherwise specified, inserts were made of polyvinylchloride plastic, which was also wet completely by the oil. The four boundary conditions we used were:

(*a*) *straight sidewalls* with completely wetting fluid (figure 4*a*);

(*b*) *brimful* conditions (Benjamin & Scott 1979; Douady 1990) (figure 4*b*);

(*c*) *sloping sides* (figure 4*c*);

(*d*) *shelf* conditions (figure 4*d*).

As discussed by Douady (1990), straight sidewalls will emit meniscus waves. Since they are directly forced waves, they vibrate at the pump frequency. Moreover, they have no threshold and can mask the true threshold for parametrically pumped waves (at $\omega/2$). Since the initial surface is no longer flat, the calculations described above are no longer strictly valid.

We made brief experiments using the brimful conditions of Benjamin & Scott (1979) and Douady (1990). The advantage of this condition is that the flat interface is a rigorous solution to the equations so that no meniscus wave is emitted. To implement this condition, one must find a sidewall material on which the oil–air interface has a finite contact angle. Both teflon and neoprene rubber had acceptable non-wetting properties, but they are far from ideal materials for machining. In practice, good alignment of the contact line with the brim is needed to eliminate the wave.

The third and fourth conditions may be viewed as ways of eliminating reflected waves by impedance matching. Since the threshold rises for shallow fluids, a gradual decrease (sloping sides) gradually reduces the effective control parameter to zero. For the shelf method, the idea was to have a very shallow shelf where parametric waves could not be excited and where the meniscus wave from the wall would damp out. Here, too, we found it better to have the shelf slope off into the full depth rather than form a sharp corner.

### 4.4. *Temperature control*

Because the viscosity of the fluid changes rapidly with temperature (see the Appendix), good temperature control is desirable. In addition, by varying the set-point temperature, we could in effect scan the fluid viscosity, which turned out to be an important

parameter to control. The entire shaker table and sample holder was enclosed in a Plexiglas can with glass top for visualization (figure 2). Since the shaker table itself dissipated a sizeable amount of heat (the coils passed 7 A of current), we inserted a small brass element with flowing water to carry off this heat. The water was temperature controlled by a waterbath (Neslab RTE 221) to 0.01 °C. Under the sample holder, we glued a film heater (Minco). A platinum RTD under the base measured the temperature and allowed feedback control by a Macintosh computer. In steady-state operation, the stability was about $\pm 0.001$ °C. However, direct measurements with a thermometer in the fluid showed that there were significant non-uniformities in the fluid itself.

We measured these when controlling the temperature of the fluid at 23 °C, with a depth of 1.0 cm. Without shaking, lateral differences were 0.1 °C. They are caused by the small size of the water cooler and can easily be eliminated (again, at the cost of a heavier sample holder). While shaking, they were less than 0.05 °C. Only a small part of the lateral inhomogeneities in the thresholds that we observed was due to these gradients.

The vertical gradients are larger and their effects harder to measure. Without shaking, vertical differences were 0.4 °C. They are due to the cooler air (21.9 °C) above the surface compared to the temperature control at 23 °C in the base. When shaking below onset (2.5 $g$ at 40 Hz), these temperature differences decreased to 0.02 °C, because of fluid mixing. Above onset (6 $g$ at 40 Hz), the vertical gradients became larger again: 0.1 °C. This might be caused by viscous dissipation at the surface of the fluid, which can be estimated as (Landau & Lifshitz 1987, p. 92)

$$\frac{\mathrm{d}E}{\mathrm{d}t} = -\tfrac{1}{2}\eta \int \left(\frac{\partial v_i}{\partial x_k} + \frac{\partial v_k}{\partial x_i}\right)^2 \mathrm{d}(vol) \sim \frac{1}{2}(\nu\rho)(v^2k^2)(L^2\lambda) \tag{4.1}$$

$$\sim \tfrac{1}{2}(\nu\rho)\left(\frac{a^2}{(\omega/2)^2}\right) L^2 2\pi \left(\frac{\rho(\omega/2)^2}{\gamma}\right)^{1/3} \sim 4^{2/3}\pi\nu\rho a^2 L^2 \frac{(\rho/\gamma)^{1/3}}{\omega^{4/3}}. \tag{4.2}$$

Here, $\lambda$ is the onset wavelength. The volume integral is calculated as though a constant shear $vk$ extended a depth $\lambda$ below the surface. The fluid velocity $v$ is estimated by its inviscid values: $v = a/(\omega/2)$. The wavenumber is converted to a frequency via (2.7). Using typical values of $\nu = 1\ \mathrm{cm^2\,s^{-1}}$, $\rho = 1\ \mathrm{g\,cm^{-3}}$, $a = 10^4\ \mathrm{cm\,s^{-2}}$, $\gamma = 30\ \mathrm{dynes\,cm^{-1}}$, and $\omega = 2\pi(50)$ Hz, we find that approximately 1 W is generated. This could account for the additional vertical gradient above onset.

When controlling the temperature of the fluid at 60 °C, vertical gradients reach 2 °C over 1.0 cm. Again, while shaking, fluid mixing reduces this difference. Since the fluid is less viscous at these temperatures, energy dissipation at the surface is smaller and has a smaller effect on the original gradient.

In conclusion, relatively large temperature differences exist in the fluid while making threshold measurements, and they cannot be easily controlled or estimated *a priori*. Overall, temperature variations in the cell are approximately 0.4 to 2 °C (depending on the working temperature). This uncertainty certainly accounts for some of the discrepancies that we observe in thresholds.

### 4.5. *Visualization*

The aluminium sample holders were sandblasted and anodized black to eliminate reflections, so that the light used for visualization reflected off the fluid surface only. A ring of 100 red LEDs 28 cm in diameter was placed above the sample at a height

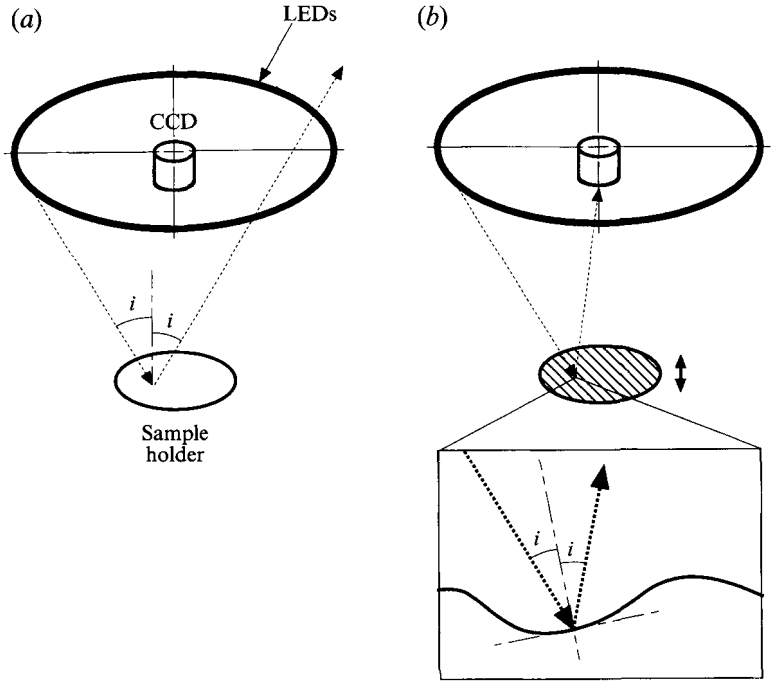


FIGURE 5. Visualization of the surface. (*a*) When the surface is flat, no light is reflected into the camera; (*b*) when it is rippled, a range of angles is visualized.

of 165 cm with a CCD camera at its centre. (See figure 5.) The radius of the ring was chosen so that no light was reflected into the camera lens from the flat fluid surface; however, an inclined surface of the proper angle will reflect light into the camera. At the ring height that we used, the angles visualized ranged from 0.7° to 4.2° over the sample surface. One concern is that since only finite-angle surface deformations are visible, the acceleration threshold will be overestimated. By lowering the height of the LED ring, we checked that these errors were negligable (less than 0.1% on the acceleration thresholds) compared to the accelerometer precision.

The illumination system could be operated continuously or strobed either at the pump frequency $\omega$ (for visualizing meniscus waves) or half the pump frequency $\omega/2$ (for visualizing parametric waves). The strobe duration was approximately 1 ms, and the phase relative to the trigger could be adjusted continuously. When strobed at $\omega/2$, stripe patterns were seen as two lines per wavelength, with the light reflected from the trough brighter than that from the crest. By strobing at $\omega$ and then $\omega/2$, one could determine whether a given pattern was harmonic (a meniscus wave) or subharmonic (a parametrically generated wave).

The advantages of this illumination system are its crisp images and the ease of their interpretation. (Since the light-emitting element of each LED is less than a millimetre square, it subtends an angle of less than $10^{-3}$ rad and light rays can be taken as coming from a one-dimensional ring.) The disadvantages are that very small-amplitude distortions cannot be seen, that one does not have a continuous image of the height displacement, and that the strobe rate could combine with the 60 Hz strobe rate of the CCD camera to give unpleasant flashing effects on the TV monitor.

## 5. Experimental results

Our first goal was to see whether we could find circumstances where the infinite-depth, infinite-width equations accurately predicted the onset acceleration and wavelength. (In the calculation sketched above in §2, this corresponds to setting $h = \infty$.) The data shown in figure 6 demonstrate that such agreement can be achieved. The sample was the round container, with a depth of 1.0 cm, and a working temperature that varied between 22.0 °C to 22.7 °C. Similar results were obtained with the various boundary conditions. The two sets of data points in figure 6(*a*) represent the lower and upper bounds on the critical acceleration. The lower bound represents the lowest acceleration at which any part of the surface had destabilized. The upper bound represents the acceleration at which the entire cell had destabilized. The two solid lines delimit the range of possible theoretical predictions based on the temperature inhomogeneities and the uncertainty in the absolute value of the viscosity (6%). To within an overall absolute accuracy of 8%, the linear-stability analysis agrees with experiment, with no parameters fit. Similarly, figure 6(*b*) shows agreement for the wavelength of the instability at onset. The dashed lines in figures 6(*a*) and 6(*b*) are the predictions based on the Mathieu equation (2.1) with the usual phenomenological damping term ($2\nu k^2$). In these experiments, the ratio $\nu k^2/(\omega/2)$ varied from 0.20 at 20 Hz to 0.43 at 70 Hz. (The inverse of this ratio is just the quality factor of the excited mode.) We have also seen that thresholds measured in vacuum match those in air. (This is not surprising, as one expects the extra dissipation to be of order $\eta_{air}/\eta_{oil} \approx 10^{-4}$.)

Such absolute agreement has been seen in only a few other experiments on hydrodynamic instabilities, for example Rayleigh–Bénard convection (Silveston 1958) and Taylor–Couette flow (Taylor 1923). (For a review of more recent measurements at and above thresholds in these systems, see Ahlers 1990.) Of course, no one doubts the validity of the Navier–Stokes equations or the general formalism of linear-stability analysis; rather, the question is whether the source of energy dissipation that has been taken into account (bulk viscosity along the surface) is sufficient to describe the fluid and whether all of the necessary restoring forces on the interface (which fix the wavelength via the dispersion relation) have been taken into account. We remind the reader that in our theoretical calculations, we have ignored dissipation due to the bottom surface, the sidewalls, the contact line, the air motion, and any surfactant film. Within our working accuracy of 8%, our data support this neglect.

Most of the uncertainty in figure 6 is systematic error. Much of it resides in the calibration of the accelerometer and in the measurement of the fluid viscosity. Most of the rest comes from temperature gradients. The first two errors may be readily reduced, but the last would require a substantial redesign of the experiment. In any case, the accuracy suffices to make our basic point: by properly choosing the fluid viscosity, the pump frequency, the cell width and depth, we can find close agreement between theory and experiment. Most of the rest of our experiments were aimed at showing systematically how complications arise as these are abandoned one by one.

The lower frequency limit to the data in figure 6 is set by the maximum displacement of our shaker table (0.8 cm), which severely limits the acceleration at low frequencies. By raising the fluid temperature (reducing the viscosity), we could explore lower frequencies, where wavelengths are longer and begin to be comparable to the fluid depth. Figure 7 shows a 0.24 cm deep fluid in the same cell, at a fluid temperature of 55.4 °C $\pm$0.6 °C. In this and the following data, we have adjusted the temperature used for our theoretical prediction (within the range given above) so that one point (at large

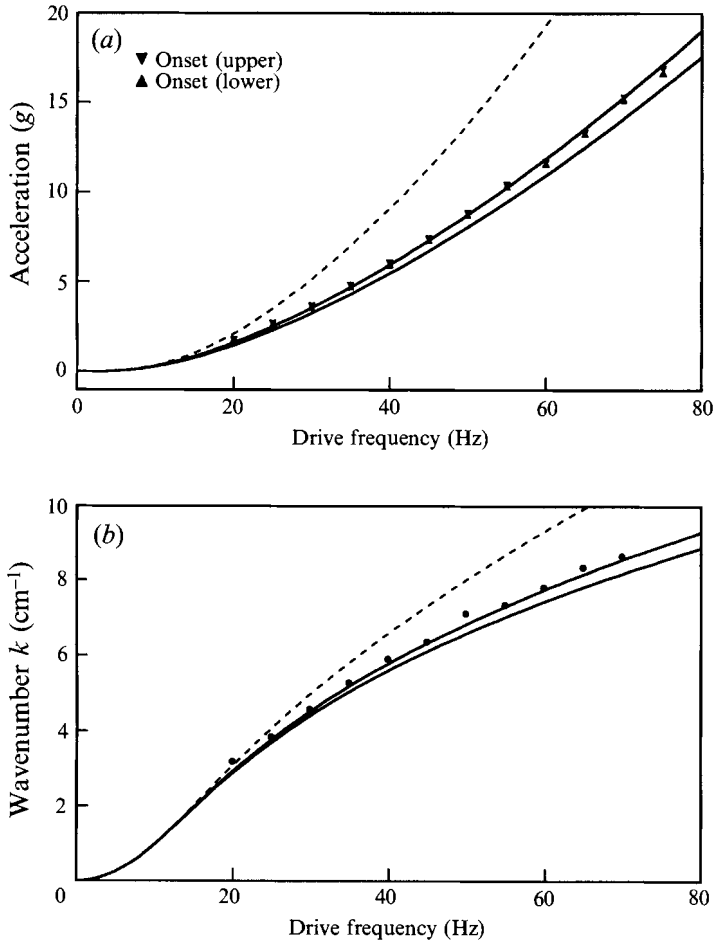


FIGURE 6. Threshold and wavelength measurements for oil at 23 °C in a round container of diameter 10 cm and depth 1.0 cm. (*a*) Acceleration thresholds. The solid lines are numerical calculations using the Kumar & Tuckerman method, taken at 21 °C (upper) and 23 °C (lower). The dashed line is an estimate based on the perturbative theory ($a_c = 4\nu k\omega$). (*b*) Wavelength just above onset. The solid lines are numerical calculations at 21 °C (lower) and 23 °C (upper), and the dashed line is the perturbative estimate (see §2). The calculations and estimates are for $h = \infty$. Boundary condition 'a' was used for these data and for the rest of the data shown in this section.

accelerations) matches the data. At the same time, we adopted a consistent criterion for the destabilization of the interface. (We defined the threshold as corresponding to destabilization everywhere in the cell.) We view this as a crude 'one-parameter' fit that eliminates the trivial calibration errors discussed above. The data in figure 7 show the high precision with which the data match the theoretical predictions. Unlike the previous case, the shallow depth means that viscous damping at the bottom of the cell cannot be neglected. Indeed, as the wavelength becomes large compared to the depth, the threshold diverges towards infinity. The dashed curve shows the infinite-depth prediction. (This curve is not the perturbative prediction discussed above; it is the same curve that agrees with the experimental data in figure 6.)

The careful reader will note a small deviation at the lowest frequencies between the data in figure 7 and the theoretical prediction. Although small, the deviations are real and significant. As we shall show, they reflect damping by the sidewalls. Figure 8,

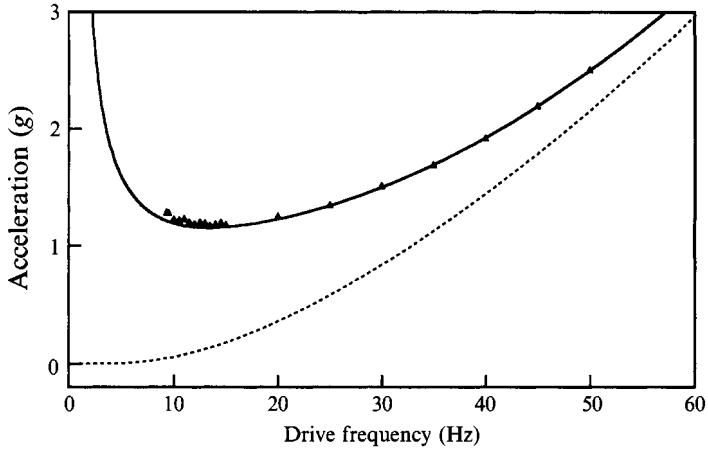


FIGURE 7. Threshold measurements for oil at 55 °C in a square container of width 11.4 cm and depth 0.24 cm. The solid line is the finite-depth numerical calculation; the dashed line is the infinite-depth one.

which differs from figure 7 in that the depth is greater, shows an instance where these deviations are large. The solid line is the finite-depth, finite-viscosity prediction; i.e. it is the same type of curve that matches the experimental data in figure 7.

Note the oscillations in the threshold that are present in ever-greater amplitude at low frequencies. (The careful reader can find hints of such oscillations in figure 7.) These oscillations are the signature of mode quantization, as mentioned at the end of §2. At higher frequencies, there is in effect a continuum of modes available to the system, since the mode spacing becomes less than the width of each mode. The mode spacing is roughly $\pi/L$, while the width of each mode is roughly

$$\Delta k \approx \pi/\ell_{decay}. \tag{5.1}$$

The condition for having a continuum of modes is thus equivalent to $L \gg \ell_{decay} \sim \gamma/4\nu\rho\omega$, as discussed in §4.1. In practice, the 'soft' boundary conditions we use increase $\Delta k$ beyond $\pi/\ell_{decay}$ and allow access to the 'infinite-cell' regime at lower frequencies than (5.1) would suggest. The threshold oscillations that we see at low frequencies are in fact the bottoms of parametric-resonance tongues (see §2 and figure 1). The small inset images in figure 8 are examples of patterns obtained at different frequencies. Each tongue corresponds to a distinct shift in observed wave pattern at onset. Patterns at higher frequencies correspond to situations where the range of modes is effectively continuous. Note that the transition from the complicated 'modal patterns' associated with each parametric-resonance tongue to squares coincides with the disappearance of oscillations in the threshold curve, reflecting the passage from a small to a large cell. Patterns in the low-frequency case are described by dynamical systems, while in the high-frequency case, they are described by amplitude equations with spatially dependent order parameters (Cross & Hohenberg 1993). The mechanism for the selection of square patterns selected by low-viscosity fluids in large cells has been previously studied experimentally and theoretically (see Milner 1991). We shall say little about the special features of small sample cells, as they have been extensively discussed before (see the references cited in the introduction).

The dashed curve in figure 8 is merely a guide to the eyes. It represents the threshold curve in the absence of mode quantization. Because the actual thresholds

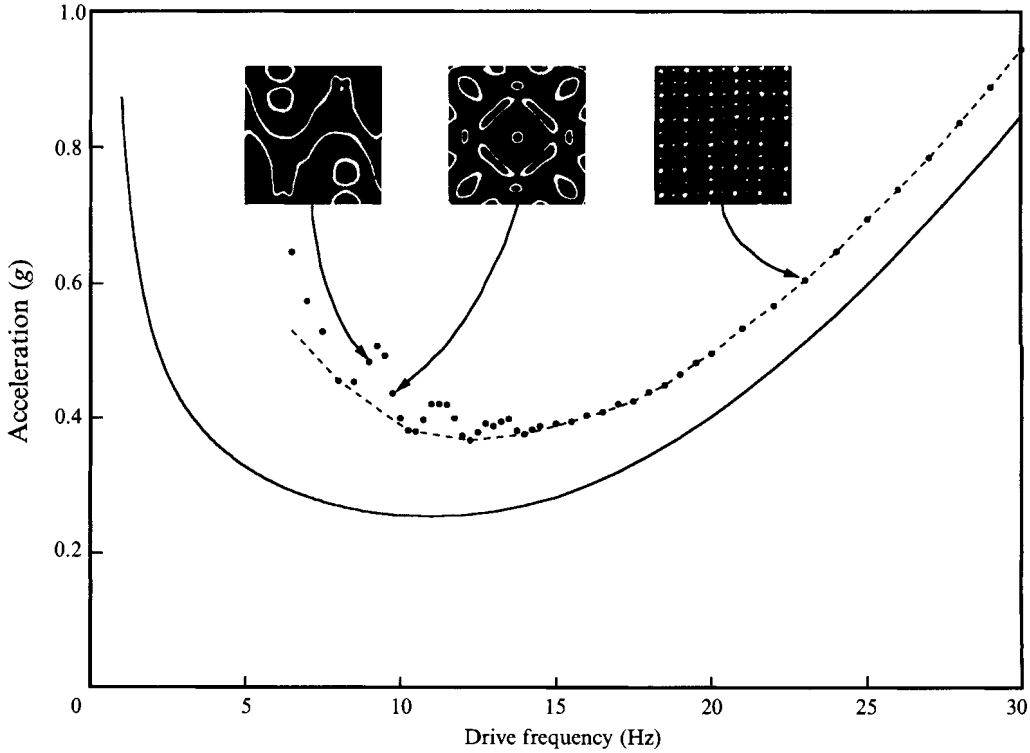


FIGURE 8. Threshold measurements for oil at 55 °C in a square container of width 11.4 cm and depth 0.7 cm. The solid line is the finite-depth numerical calculation. The dashed line represents the threshold curve in the absence of mode quantization (only the tongue minima are shown). The insets show wave patterns at onset for different frequencies.

are larger than the predictions, we conclude that another source of energy dissipation is present. Although it is possible to calculate the dashed curve from first principles, we have not tried to do so. The only situation that one could imagine treating precisely is the brimful boundary condition. For convenience, most of our work did not use this condition. As mentioned in §2, the other boundary conditions all lead to meniscus waves that invalidate the stationary solution assumed in the linear-stability analysis. Thus, not only would it become necessary to find a set of eigenfunctions that obey the sidewall conditions, it would also be necessary to perturb off a complicated initial state. Faced with these difficulties, we chose to explore the nature of the extra dissipation experimentally.

Figure 9(*a*) shows three threshold curves taken at different sample widths in otherwise-identical circumstances. Here, we have removed all points from the sides of the tongues for clarification (i.e. we have left only those points that correspond to the bottom of the tongues). Note that the smaller the fluid cell, the greater the dissipation. In figure 9(*b*), we see too that the tongue oscillations increase as the cell is made smaller, reflecting the relative paucity of modes in smaller containers.

Figures 10(*a*) and 10(*b*) show similar measurements for fixed cell size (11.4 cm) and varying fluid depths. As the fluid is made shallower, the deviation from the predicted curves decreases (figure 10*a*). The deeper cells show larger oscillations (figure 10*b*). We can qualitatively explain why the oscillations are larger by recalling that for shallow cells, the added dissipation due to shear at the bottom of the cell will broaden

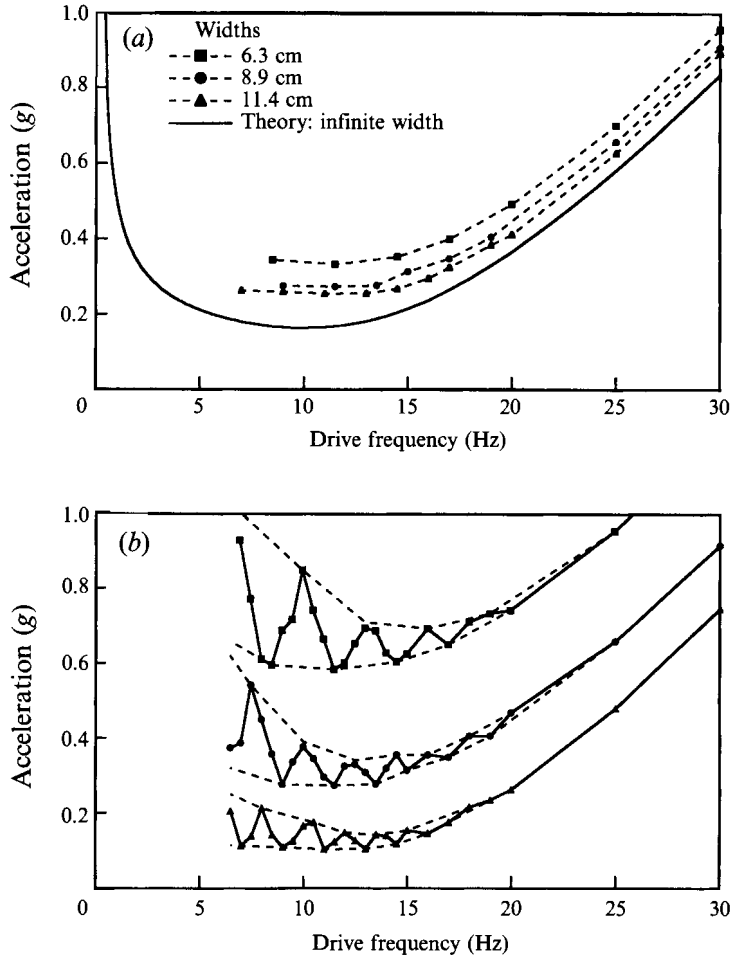


FIGURE 9. Threshold measurements for oil at 55 °C in a square container of depth 1.0 cm and varying width. (*a*) As in figure 8, only the minima of the oscillations at low frequency are shown. (*b*) Oscillations at low frequency (complete data). The dashed lines, outlining the extrema of the oscillations, are guides to the eyes. For this figure, the 6.3 cm width curve was offset by +0.25 *g* , the 11.4 cm width curve by −0.15 *g* to aid visualization.

the resonance tongues. This will tend to wash out the deviations from the threshold envelope curve, for much the same reason that the frequency response of ordinary simple harmonic resonance broadens when the damping is large.

To summarize these observations, we can define a rough measure of the deviation from theoretical predictions. Let $a_t$ be the minimum value of the accleration threshold for the theoretical prediction. Let $a_e$ be the minimum value of the experimentally measured acceleration threshold (not necessarily at the same frequency as $a_t$). Then, we define the relative deviation $D \equiv |a_t - a_e|/a_t$. In figure 11, we plot $D$ against the ratio $h/L$, where $h$ is the fluid depth and $L$ the square container size. In § 6, we argue that dissipation at the sidewalls can account for this extra deviation. (Since the fluid wets the sidewalls in these experiments, there is no anomalous contact-line dissipation. Any surface contamination would have prevented the agreement seen in the high-frequency data.)

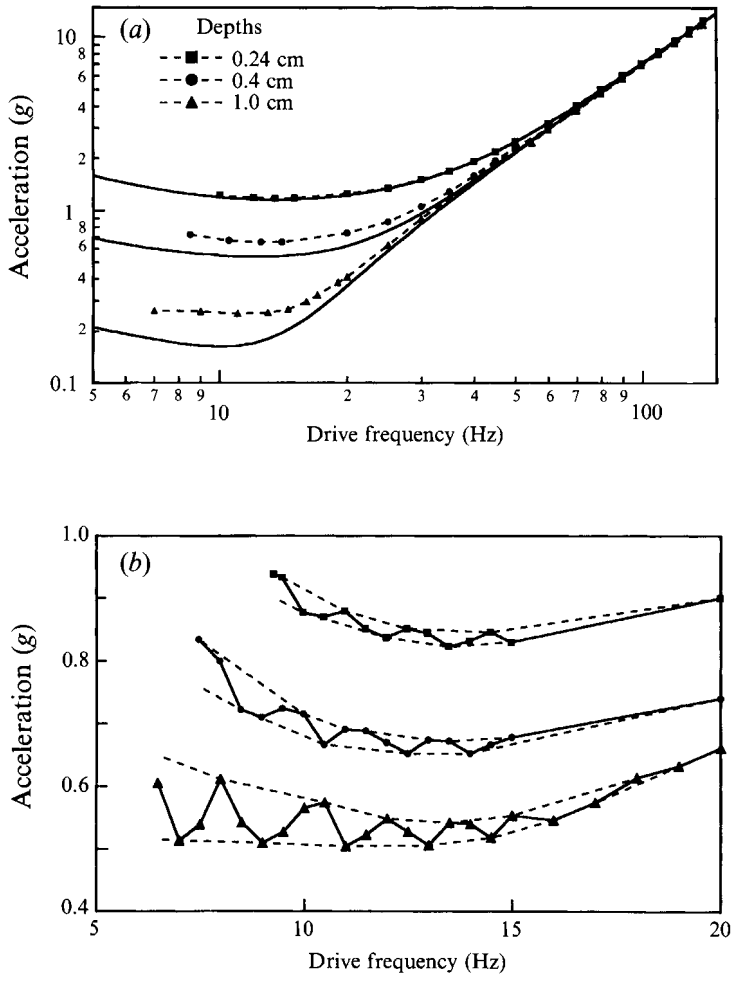


FIGURE 10. Threshold measurements for oil at 55 °C in a square container of width 11.4 cm and varying depth. (*a*) Log-log plot of the acceleration thresholds. As in figures 8 and 9(*a*), only the minima of the oscillations at low frequency are shown. (*b*) Oscillations at low frequency (complete data). For this figure, the 0.24 cm depth curve was offset by −0.35 *g*, the 1.0 cm depth curve by +0.25 *g* to aid visualization.

## 6. Discussion

We have shown that the theoretical model of Kumar & Tuckerman (1994) agrees quantitatively with experimental observation when a number of precautions are observed. These precautions are that

1. the surface tension is low enough to prevent contamination by an adsorbed layer of molecules;

2. the frequency is high enough and the ratio $h/L$ is small enough.

At any given depth, we can always go to an 'infinite-width' limit by making the frequency large enough. (See figure 10*a*.) We also see that the ratio $h/L$ must be made small. (Just how small depends on the operating frequency. The measure of deviation discussed above is a worst-case scenario because we have scanned frequencies. At higher frequencies, the deviations are smaller in any given situation.)

Although there are good reasons for making $h/L$ small, there are also reasons for

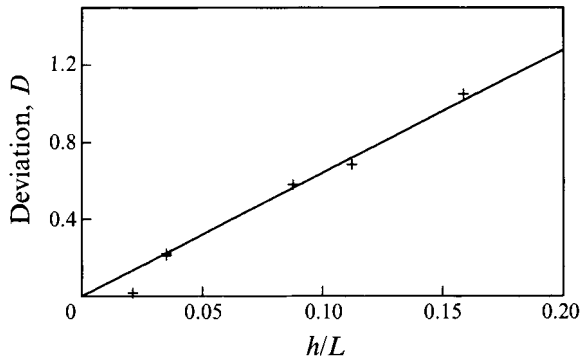


FIGURE 11. Deviation of experimental data from theoretical predictions. The estimate $D = |a_t - a_e|/a_t$ is used, and the results were fit to a line.

not making the depth too small. If one can place oneself in the situation of figure 6, then the infinite-depth calculations may be relevant. While there may not seem to be any need to do this for threshold measurements, this may be useful for modelling nonlinear phenomena. (Note the enormous difference in complexity between the infinite- and finite-depth dispersion relations.) Of course, one must still check whether depth effects are important for large wave amplitudes. At threshold, the depth may be effectively infinite while above threshold the finite depth may become important.

We conclude, too, that the very shallow depths (0.2 to 0.3 cm) used by Edwards & Fauve (1993) and Müller (1993) are perhaps overly conservative. The fluid can be deep enough that the thresholds at the desired frequencies are essentially at their infinite-depth values, while at the same time shallow enough that long-wavelength perturbations are still strongly damped. To give an explicit example (using the estimates of damping rates at shallow depths given below), if we use our oil at 55 °C, with an excitation frequency of 50 Hz, a cell size of 12 cm and a depth of 0.4 cm, the onset acceleration predicted by the finite-depth theory exceeds the infinite-depth result by only 0.4%. Here, the damping rate of the longest possible wavelength roughly equals $\omega$ and thus these wavelengths decay rapidly. For a depth of 0.24 cm, the onset acceleration exceeds the infinite-depth prediction by 16%. Edwards & Fauve argued that for deep fluids in wide basins, long-wavelength modes would be damped so slowly that one would need to couple them to the amplitude equations near onset. Although their argument is valid, they perhaps over-estimated the shallowness actually needed to avoid long-wavelength dynamics.

A crude argument to understand why the relative deviations from the model are proportional to $h/L$ can be constructed in analogy to that used by Milner (1991) to estimate wall damping for infinite depth. The goal is to estimate the ratio between the damping rate due to sidewall friction and that due to damping over the entire free surface. For shallow fluids, we expect, following (4.1), that the energy dissipation due to the sidewalls is

$$\frac{\mathrm{d}E}{\mathrm{d}t} \sim (\rho\nu)(Lh^2)\left(\frac{v^2}{h^2}\right) \sim (\rho\nu)(Lv^2), \tag{6.1}$$

where the shear rate is $v/h$ ($v$ the fluid velocity, $h$ the depth), and we have assumed that the wall damping extends throughout the depth of the cell and to a distance away from the walls equal to the depth. (This last assumption is perhaps the most

tenuous of those made.) The energy stored in the fluid is

$$E \sim \rho v^2 (L^2 h), \tag{6.2}$$

where we have assumed that 'surface waves' dissipate energy over the entire fluid volume $L^2 h$. The ratio of these two quantities gives the damping rate due to the walls,

$$\mu_W \approx \frac{\dot{E}}{E} \sim \frac{v}{Lh}. \tag{6.3}$$

The sidewall damping is to be compared to the damping at the free surface for waves whose wavelength equals the depth. (In our definition of the 'deviation', we scanned frequencies and selected the frequency at which the finite-depth effects are significant.) The expression (4.1) is modified by replacing $k$ with $h^{-1}$, leading to $\mu \sim v/h^2$.

The ratio of the damping to the walls to the damping at the free surface is

$$\frac{\mu_W}{\mu} \sim \frac{v}{Lh} \frac{h^2}{v} \sim \frac{h}{L}, \tag{6.4}$$

which is the experimental result. For small $h/L$, we can thus neglect sidewall damping.

Finally, we note that there are definite advantages to using high-viscosity fluids. As Edwards & Fauve (1993) have argued, for low-viscosity fluids, the coherence length $\xi$ of wave oscillations is many times the actual wavelength. (The coherence length may be defined to be $2\pi/\Delta k$, where $\Delta k$ is the range of wavenumbers that are unstable to infinitesimal perturbations. Physically, $\xi$ is roughly the decay length $\ell_{decay}$ discussed in §§4.1 and 5.) The aspect ratio of the system, which measures how many independent 'patterns' will fit into the sample geometry, is properly defined to be the ratio of the system size $L$ to the coherence length $\xi$ and not $L/\lambda$.

In figure 12, we use the tongues found in figure 1 to plot the ratio of $\xi$ to $\lambda$ as a function of the distance above onset. Near onset, the ratio is always large because of well-known critical effects in the vicinity of a forward bifurcation. Farther above onset, we see that for water at 20 °C, this ratio is several hundred, while for our oil it becomes close to one. If the bare correlation length is large compared to $\lambda$, then even far above onset, there will be correlations over long lengths. This has important implications for the interpretation of Faraday experiments on low-viscosity fluids, such as those by Christiansen *et al.* (1992) and Gluckman *et al.* (1993). In the former, standing wave resonances of 3, 4, 5, and higher numbers of waves were formed by reflecting off the walls of a circular container. In the latter, it was observed that even when the wave pattern was highly disordered, the boundaries nonetheless managed to influence the pattern over the entire cell via a 'phase rigidity' that was clearly seen by averaging many images of the interface (cf. Cross & Hohenberg 1993, pp. 882–883 for a discussion of the phase as a 'rigid' variable). In retrospect, the unusual features of these experiments, as compared to, say, convection, come from having been conducted in this new limit of pattern formation. It would be interesting to see if by multi-scale analysis one can derive appropriate asymptotic equations that capture the combination of slow spatial and fast temporal variations that these patterns display.

## 7. Conclusion

We have conducted systematic measurements of the threshold accelerations in the Faraday experiment, using a viscous, non-polar fluid. By proper experimental

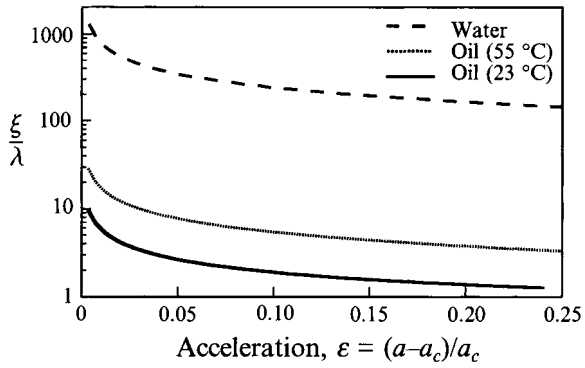


FIGURE 12. Ratio of the coherence length to the wavelength, calculated by the Kumar & Tuckerman method. As $\varepsilon \to 0$, the ratio diverges because we are near the bottom of a resonance tongue and $\Delta k$ is small. This is the analogue in pattern formation of the well-known divergence of the correlation length in critical phenomena.

design, the sources of dissipation that determine these thresholds may be controlled. In particular, we see when damping at the bottom and sides of the cell becomes important and when it may be neglected. By using a non-polar fluid, we avoid problems of surface contamination. An understanding of the linear-stability analysis is important not only to check the physical models employed but also to design experiments to be conducted in the nonlinear regime. Misunderstanding of the linear problem has led to some confusion over the interpretation of previous experiments. On the positive side, we have used the insights gained in this analysis to explore secondary instabilities in the Faraday experiment. We hope to report on these in the near future.

This research was partially funded by an NSERC Research Grant. J. B. gratefully acknowledges an Alfred P. Sloan fellowship. V. E. and S. M. acknowledge funding from the Ecole Normale Supérieure (Paris). A first version of the experimental apparatus was built by Ed Levinson and Julien Prieur; their insights helped set the design of the present apparatus. Stuart Edwards and Laurette Tuckerman are thanked for useful conversations.

## Appendix. Measurement of fluid properties

One advantage of measuring fluid properties 'in-house' is that the same temperature scale is used for both the measurements and the actual experiments. In view of the large temperature dependence of the viscosity, this is important. The temperature scales used in our experiment were compared against a standard platinum resistance and have an absolute accuracy of about 0.2 °C. Below, we describe separately measurements of density, surface tension, and viscosity.

### A.1. *Density*

The density was measured using a 250 ml volumetric flask. The fluid level was adjusted while the flask was immersed in a water bath at the desired temperature. The flask was removed from the bath, dried in an oven, and weighed. (Since pump oil has a low vapour pressure, there was no problem of evaporation.) Our results are shown in figure 13(*a*) and were fit to a straight line. Fit residuals were about 0.1%.

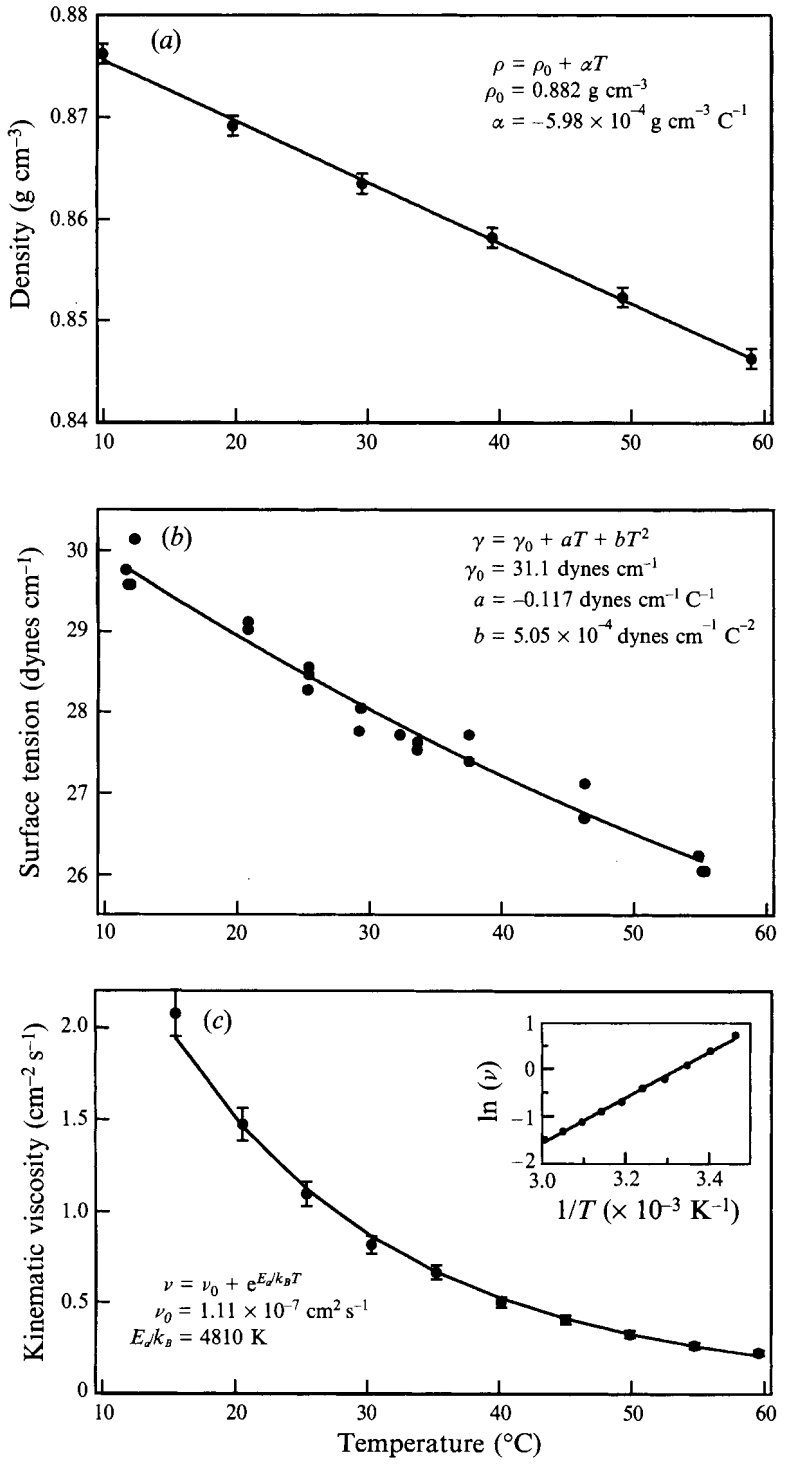


FIGURE 13. (*a*) Density measurements for the oil. (*b*) Surface tension measurements for the oil. (*c*) Kinematic viscosity measurements for the oil.

### A.2. *Surface tension*

The surface tension was measured using the ring method (Adamson 1990, pp. 23–25). The torque needed to lift off a ring of platinum wire is measured by a standard apparatus (Fisher Surface Tensiometer Model 20). The temperature of the oil was varied by placing it in a beaker with a circulating water jacket; the actual surface tension was measured for different bath temperatures. The results are shown in figure 13(*b*) and were fit to a quadratic polynomial. Fit residuals were about 1%.

### A.3. *Viscosity*

The viscosity $\eta$ was measured by the Ostwald method (Hatschek 1928, pp. 24-29), which in effect measures the velocity of Poiseuille flow. The measurement is relative to a known fluid (toluene). To do this, the velocity of the trailing meniscus of the fluid is measured by timing its fall past two sets of LEDs and photodiodes. The idea is to make the flow pass through a narrow capillary tube, whose viscous dissipation dominates over other parts of the cell. The whole apparatus is surrounded by temperature-controlled water. Our measurements were converted to kinematic viscosities $\nu = \eta/\rho$ and are shown in figure 13(*c*). They were fit to an Arrhenius formula (Nagel 1991, p. 131). Fit residuals were about 6%, which is roughly the absolute accuracy that we observed for measurements on toluene.

## REFERENCES


ADAMSON, A. W. 1990 *Physical Chemistry of Surfaces,* 5th edn. Wiley Interscience.

AHLERS, G. 1990 Experiments on bifurcations and one-dimensional patterns in non-equilibrium systems far from equilibrium. In *Lectures in the Sciences of Complexity* (ed. D. Stein), pp. 175–224. Addison–Wesley.

BENJAMIN, T. B. & SCOTT, J. C. 1979 Gravity–capillary waves with edge constraints. *J. Fluid Mech.* **92**, 241–267.

BENJAMIN, T. B. & URSELL, F. 1954 The stability of the plane free surface of a liquid in vertical periodic motion. *Proc. R. Soc. Lond.* A **225**, 505–515.

BOSCH, E. & WATER, W. VAN DE 1993 Spatiotemporal intermittency in the Faraday experiment. *Phys. Rev. Lett.* **70**, 3420–3423.

CHRISTIANSEN, B., ALSTROM, P. & LEVINSEN, M. 1992 Ordered capillary-wave states: quasicrystals, hexagons, and radial waves. *Phys. Rev. Lett.* **68**, 2157–2160.

CHRISTIANSEN, B., ALSTROM, P. & LEVINSEN, M. 1995 Dissipation and ordering in capillary waves at high aspect ratios. *J. Fluid Mech.*, in press.

CILIBERTO, S. & GOLLUB, J. P. 1984 Pattern competition leads to chaos. *Phys. Rev. Lett.* **52**, 922–925.

CILIBERTO, S. & GOLLUB, J. P. 1985 Chaotic mode competition in parametrically forced surface waves. *J. Fluid Mech.* **158**, 381–398.

CROSS, M. C. & HOHENBERG, P. C. 1993 Pattern formation outside of equilibrium. *Rev. Mod. Phys.* **65**, 851–1112.

DOUADY, S. 1990 Experimental study of the Faraday instability. *J. Fluid Mech.* **221**, 383–409.

DOUADY, S. & FAUVE, S. 1988 Pattern selection in Faraday instability. *Europhys. Lett.* **6**, 221–226.

EDWARDS, W. S. & FAUVE, S. 1992 Structure quasicrystalline engendrée par instabilité paramétrique. *C. R. Acad. Sci. Paris, II* **315**, 417–420.

EDWARDS, W. S. & FAUVE, S. 1993 Parametrically excited quasicrystalline surface waves. *Phys. Rev.* E **47**, 788–791.

EDWARDS, W. S. & FAUVE, S. 1994 Patterns and quasi-patterns in the Faraday experiment. *J. Fluid Mech.* **278**, 123–148.

EZERSKII, A. B., KOROTIN, P. I. & RABINOVICH, M. I. 1985 Random self-modulation of two-dimensional structures on a liquid surface during parametric excitation. *Zh. Eksp. Teor. Fiz.* **41**, 129-131 (transl. 1986 *Sov. Phys. JETP* **41**, 157–160).

FARADAY, M. 1831 On the forms and states assumed by fluids in contact with vibrating elastic surfaces. *Phil. Trans. R. Soc. Lond.* **52**, 319–340.

FAUVE, S., KUMAR, K., LAROCHE, C., BEYSENS, D. & GARRABOS, Y. 1992 Parametric instability of a liquid–vapor interface close to the critical point. *Phys. Rev. Lett.* **68**, 3160–3163.

GLUCKMAN, B. J., MARCQ, P., BRIDGER, J. & GOLLUB, J. P. 1993 Time averaging of chaotic spatiotemporal wave patterns. *Phys. Rev. Lett.* **71**, 2034–2037.

GOLDSTEIN, H. 1980 *Classical Mechanics,* 2nd edn. Addison–Wesley.

GOLLUB, J. P. 1991 Nonlinear waves: dynamics and transport. *Physica* D **51**, 501–511.

GOLLUB, J. P. & MEYER, C. W. 1983 Symmetry breaking instabilities on a fluid surface. *Physica* D **6**, 337–346.

HATSCHEK, E. 1928 *The Viscosity of Liquids.* D. van Nostrand.

HENDERSON, D. M. & MILES, J. W. 1990 Single-mode Faraday waves in small cylinders. *J. Fluid Mech.* **213**, 95–109.

HOCKING, L. M. 1987 The damping of capillary–gravity waves at a rigid boundary. *J. Fluid Mech.* **179**, 253–266.

KUMAR, K. & TUCKERMAN, L. S. 1994 Parametric instability of the interface between two fluids. *J. Fluid Mech.* **279**, 49–68.

LAMB, H. 1932 *Hydrodynamics,* 6th edn. Cambridge University Press. Reprinted Dover Publications, 1945.

LANDAU, L. D. & LIFSHITZ, E. M. 1976 *Mechanics,* 3rd edn. Pergamon.

LANDAU, L. D. & LIFSHITZ, E. M. 1987 *Fluid Mechanics,* 2nd edn. Pergamon.

MILES, J. W. 1967 Surface-wave damping in closed basins. *Proc. R. Soc. Lond.* A **297**, 459–475.

MILES, J. W. 1992 On Rayleigh's investigation of crispations of fluid resting on a vibrating support. *J. Fluid Mech.* **244**, 645–648.

MILES, J. W. 1993 On Faraday waves. *J. Fluid Mech.* **248**, 671–683.

MILES, J. W. & HENDERSON, D. 1990 Parametrically forced surface waves. *Ann. Rev. Fluid Mech.* **22**, 143–165.

MILNER, S. T. 1991 Square patterns and secondary instabilities in driven capillary waves. *J. Fluid Mech.* **225**, 81–100.

MÜLLER, H. W. 1993 Periodic triangular patterns in the Faraday experiment. *Phys. Rev. Lett.* **71**, 3287–3290.

NAGEL, S. R. 1991 Experimental analysis of disordered systems. In *1990 Lectures in Complex Systems* (ed. L. Nadel & D. L. Stein), pp. 125-161. Addison-Wesley.

NEVOLIN, V. G. 1984 Parametric excitation of surface waves. *Inzhenerno-Fiz. Zhu.* **47**, 1028–1042 (transl. *J. Engng Phys.* (1985) **49**, 1482–1494).

RAYLEIGH, LORD 1883*a* On maintained vibrations. *Phi. Mag.* **15**, 229–235. Reprinted in *Scientific Papers by Lord Rayleigh*, Vol. II, pp. 188–193. Dover, 1964

RAYLEIGH, LORD 1883*b* On the crispations of fluid resting upon a vibrating support. *Phi. Mag.* **16**, 50–58. Reprinted in *Scientific Papers by Lord Rayleigh*, Vol. II, pp. 212–219. Dover, 1964

SEGEL, L. A. 1977 *Mathematics Applied to Continuum Mechanics.* Macmillan. Reprinted Dover 1987.

SILVESTON, P. L. 1958 Wärmedurchgang in waagerechten Flüssigkeitsschichten. *Forsch. Ing. Wes.* **24**, 29–32, 59–69.

SIMONELLI, F. & GOLLUB, J. P. 1989 Surface wave mode interactions: effects of symmetry and degeneracy. *J. Fluid Mech.* **199**, 471–494.

TANFORD, C. 1989 *Ben Franklin Stilled the Waves.* Duke.

TAYLOR, G. I. 1923 Stability of a viscous fluid contained between two rotating cylinders. *Phil. Trans. Roy. Soc. Lond.* A **223**, 289–343.

TUFILLARO, N. B., RAMSHANKAR, R. & GOLLUB, J. P. 1989 Order–disorder transition in capillary ripples. *Phys. Rev. Lett.* **62**, 422–425.

URSELL, F. 1952 Edge waves on a sloping beach. *Proc. R. Soc. Lond.* A **214**, 79–97.